




Narrow-gap semiconducting behavior in antiferromagnetic $\text{Eu}_{11}\text{InSb}_9$ S. S. Fender , S. M. Thomas , F. Ronning, E. D. Bauer, J. D. Thompson, and P. F. S. Rosa 
MPA-Q, Los Alamos National Laboratory, Los Alamos, New Mexico 87545, USA

(Received 11 May 2021; accepted 14 July 2021; published 29 July 2021)

Here we investigate the thermodynamic and electronic properties of $\text{Eu}_{11}\text{InSb}_9$ single crystals. Electrical transport data show that $\text{Eu}_{11}\text{InSb}_9$ has a semiconducting ground state with a relatively narrow band gap of 320 meV. Magnetic susceptibility data reveal antiferromagnetic order at low temperatures, whereas ferromagnetic interactions dominate at high temperature. Specific heat, magnetic susceptibility, and electrical resistivity measurements reveal three phase transitions at $T_{N1} = 9.3$ K, $T_{N2} = 8.3$ K, and $T_{N3} = 4.3$ K. Unlike $\text{Eu}_5\text{In}_2\text{Sb}_6$, a related europium-containing Zintl compound, no colossal magnetoresistance (CMR) is observed in $\text{Eu}_{11}\text{InSb}_9$. We attribute the absence of CMR to the smaller carrier density and the larger distance between Eu ions and In-Sb polyhedra in $\text{Eu}_{11}\text{InSb}_9$. Our results indicate that $\text{Eu}_{11}\text{InSb}_9$ has potential applications as a thermoelectric material through doping or as a long-wavelength detector due to its narrow gap.

DOI: [10.1103/PhysRevMaterials.5.074603](https://doi.org/10.1103/PhysRevMaterials.5.074603)

I. INTRODUCTION

Narrow-gap semiconductors have drawn renewed interest due to a number of promising applications, which include thermoelectric devices and photoelectrodes, dark matter detectors, and quantum computing platforms based on topological properties [1–5]. These diverse applications rely on the discovery of new, stable, and clean candidates. Zintl-phase materials are a particularly promising route in the design of narrow-gap semiconductors owing to their inherent charge balance. Zintl intermetallic phases are a combination of alkaline, alkaline-earth, or rare-earth cations and a covalently bonded polyanionic structure that achieves an octet in the valence electron shell [6]. Zintl compounds are valence precise, and electron transfer between cations and anions is expected to create a semiconducting state [7]. Further, the inclusion of rare-earth elements with localized f electrons may enable magnetic order and reduce sensitivity to air and moisture compared to their alkaline and alkaline-earth analogs [8–10].

The large number of narrow-gap semiconductors reported within the Zintl concept points to a promising pathway to realizing new narrow-gap materials. For instance, investigations of $\text{Yb}_{11}\text{GaSb}_9$, $\text{Yb}_{11}\text{InSb}_9$, $\text{Yb}_{11}\text{AlSb}_9$, $\text{Ca}_{11}\text{AlSb}_9$, and $\text{Sr}_{11}\text{AlSb}_9$ support the notion that the Zintl formalism gives rise to a narrow-gap semiconducting state [11–13]. Notably, $\text{Yb}_{11}\text{GaSb}_9$ displays semiconducting behavior in electrical resistivity, but the presence of significant sample dependence indicates that impurity states play a role, e.g., small amounts of Yb^{3+} from Yb_2O_3 [14]. Conversely, isostructural $\text{Eu}_{11}\text{InSb}_9$ was reported to be paramagnetic above 8 K, which is unusual given the expected divalent europium configuration, and its electrical resistance showed a weakly metallic behavior, which marks a distinct deviation from the Zintl formalism in this family [9].

Useful insights can be obtained by comparison with structurally related compounds. For example, $\text{Eu}_5\text{In}_2\text{Sb}_6$ and

$\text{Yb}_5\text{In}_2\text{Sb}_6$ are narrow-gap semiconductors that satisfy the Zintl formalism and show promise as thermoelectric materials [10,15]. $\text{Eu}_5\text{In}_2\text{Sb}_6$ also undergoes a dramatic reduction in electrical resistance in the presence of magnetic fields [8]. This property, initially observed in perovskite manganites, is coined colossal magnetoresistance (CMR) [16] and has been attributed to the presence of magnetic polarons, i.e., quasiparticles arising from strong exchange coupling between free carriers and background spins of divalent europium. The large negative magnetoresistance in $\text{Eu}_5\text{In}_2\text{Sb}_6$ is among the largest CMR observed to date, which invites further investigation of Eu-containing narrow-gap materials [18–22].

Here we investigate the structural and physical properties of $\text{Eu}_{11}\text{InSb}_9$ single crystals grown by the self-flux method. $\text{Eu}_{11}\text{InSb}_9$ crystallizes in an orthorhombic crystal structure displaying nonsymmorphic symmetries but no inversion symmetry (space group 45, $Iba2$). In this structure, six inequivalent europium sites are located between polyanionic InSb_4 tetrahedra, Sb_2 dimers, and Sb ions. To achieve charge balance, europium ions are expected to be divalent in line with $[\text{11Eu}^{2+}][\text{InSb}_4^{9-}][\text{Sb}_2^{4-}][\text{3(Sb}^{3-})]$. Because Eu^{2+} ions have a large local moment, this electron count indicates that $\text{Eu}_{11}\text{InSb}_9$ will likely order magnetically. In fact, our magnetic susceptibility and specific heat results show that $\text{Eu}_{11}\text{InSb}_9$ has a complex magnetic ground state and undergoes three magnetic phase transitions at $T_{N1} = 9.3$ K, $T_{N2} = 8.3$ K, and $T_{N3} = 4.3$ K. Both the entropy recovered at the magnetic transitions and the high-temperature Weiss temperature are consistent with divalent europium. In addition, our electrical resistivity data display a relatively small activation energy of 160 meV and a low carrier density of 10^{15} holes/cm³, which are consistent with narrow-gap semiconducting behavior. At low temperatures, however, a departure from the activated behavior points to the presence of in-gap conducting channels. Compared to $\text{Eu}_5\text{In}_2\text{Sb}_6$, the coupling between f and conduction electrons in $\text{Eu}_{11}\text{InSb}_9$ appears to be much

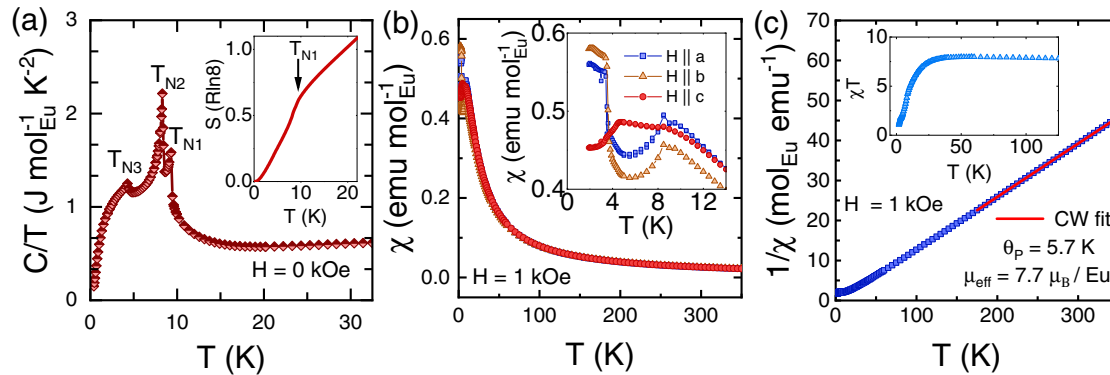


FIG. 1. (a) Specific heat divided by temperature T , C/T vs T , at zero magnetic field of $\text{Eu}_{11}\text{InSb}_9$. The inset displays the entropy in units of $R\ln 8$. (b) Temperature dependent magnetic susceptibility $\chi(T)$ with a field of 1 kOe applied along distinct crystallographic directions. The inset shows the low-temperature anisotropic $\chi(T)$ data. (c) Inverse magnetic susceptibility $1/\chi(T)$ vs T . A Curie-Weiss fit is shown by a solid line. The inset shows χT as a function of temperature.

smaller, and colossal magnetoresistance is not observed. We discuss possible origins for the small magnetoresistance of $\text{Eu}_{11}\text{InSb}_9$. Our results show that $\text{Eu}_{11}\text{InSb}_9$ is a magnetically ordered Zintl semiconductor and invite further investigation of its thermoelectric and long-wavelength detector properties.

II. EXPERIMENTAL DETAILS

Single crystals of $\text{Eu}_{11}\text{InSb}_9$ were grown through a self-flux of constituent elements in excess indium with an elemental precursor stoichiometry of $10\text{Eu}:60\text{In}:8\text{Sb}$. The elements were placed in an alumina crucible with a quartz wool filter and then sealed in a silica ampule under partial argon pressure. The ampule was heated to 1050°C over the course of 14 hours, held at constant temperature for 24 h, and then cooled to 750°C at $4^\circ\text{C}/\text{h}$. The flux was subsequently removed by centrifugation.

The crystallographic structure of $\text{Eu}_{11}\text{InSb}_9$ was determined at room temperature by a Bruker D8 Venture single-crystal diffractometer equipped with Mo radiation. Diffraction analysis shows that $\text{Eu}_{11}\text{InSb}_9$ crystallizes in the orthorhombic space group $Iba2$ with lattice parameters $a = 12.24 \text{ \AA}$, $b = 12.87 \text{ \AA}$, and $c = 17.32 \text{ \AA}$. These values match previous structural reports [9]. Elemental analysis using energy-dispersive x-ray spectroscopy in a FEI Quanta scanning electron microscope resulted in $\text{Eu}_{11}\text{In}_{1.3(2)}\text{Sb}_{8.9(2)}$. Single crystals of $\text{Eu}_{11}\text{InSb}_9$ are significantly less sensitive to air and moisture than the alkaline-earth counterparts, but they were kept in an argon glovebox between measurements to allow for sample stability over several months. Magnetization measurements were obtained through a Quantum Design superconductor quantum interference device-based magnetometer with 10^{-8} emu sensitivity. Specific heat measurements were made using a Quantum Design calorimeter that utilizes a quasiadiabatic thermal relaxation technique. The electrical resistivity (ρ) was measured using a standard four-probe configuration. Due to the poor conductivity of the crystals, spot welding was not possible. Pt wires were attached to sputtered gold pads using silver paint. At high temperatures, ρ was measured with a Lakeshore 372 AC bridge, whereas at low temperatures a two-point DC method was required due to the large resistance of the sample.

III. RESULTS

First, we devote our attention to the thermodynamic characterization of $\text{Eu}_{11}\text{InSb}_9$. Zero-field heat capacity as a function of temperature is shown in Fig. 1(a). Three transitions are identified at $T_{N1} = 9.3 \text{ K}$, $T_{N2} = 8.3 \text{ K}$, and $T_{N3} = 4.3 \text{ K}$. As shown in the inset of Fig. 1, the entropy recovered at T_{N1} is only 60% of the expected entropy for the $J = S = 7/2$ divalent europium multiplet, and the full $R\ln 8$ entropy is only recovered at $\sim 20 \text{ K}$. A similar entropy reduction has been observed in Zintl antiferromagnet $\text{Eu}_3\text{Sn}_2\text{P}_4$, which also hosts divalent europium [23]. The missing entropy at T_{N1} could be either caused by the presence of short-range interactions or by nonordered europium ions. Though the subtraction of a nonmagnetic phonon background is required for a more quantitative analysis, we note that the missing entropy of 40% of $R\ln 8$ is consistent with 4 out of 11 Eu ions not participating in magnetic order.

Figure 1(b) shows the magnetic susceptibility, $\chi = M/H$, of $\text{Eu}_{11}\text{InSb}_9$ as a function of temperature. As expected for Eu^{2+} , the susceptibility is isotropic at high temperature, whereas the inset of Fig. 1(b) highlights the anisotropic behavior of $\chi(T)$ in the vicinity of magnetic order. Kinks in $\chi(T)$ at $T_{N1} = 9.4 \text{ K}$, $T_{N2} = 8.4 \text{ K}$, and $T_{N3} = 4.0 \text{ K}$ reflect phase transitions, in good agreement with the transition temperatures identified in specific heat data. The inverse susceptibility $1/\chi$ as a function of temperature follows a Curie-Weiss law at high temperature ($T > 175 \text{ K}$), the results of which are shown in Fig. 1(c). The linear fit yields a positive Weiss temperature $\theta = 5.7 \text{ K}$, which indicates the presence of ferromagnetic interactions. At low temperatures ($T < 30 \text{ K}$), the deviation from Curie-Weiss behavior reflects the onset of short-ranged antiferromagnetic correlations among magnetic moments. The presence of both ferro- and antiferromagnetic interactions, as well as the presence of six inequivalent Eu sites, gives rise to a complex magnetic network with multiple exchange parameters as also observed in $\text{Eu}_5\text{In}_2\text{Sb}_6$ [8]. From the high-temperature Curie-Weiss fit, the effective moment in $\text{Eu}_{11}\text{InSb}_9$ is $7.7 \mu_B/\text{Eu}$, which is within 3% of $7.94 \mu_B$ expected for a Hund's-rule divalent europium ion. Thus, any crystal-field and Kondo effects are negligible, and the deviation at 30 K can be attributed solely to the onset of antiferromagnetic short-range

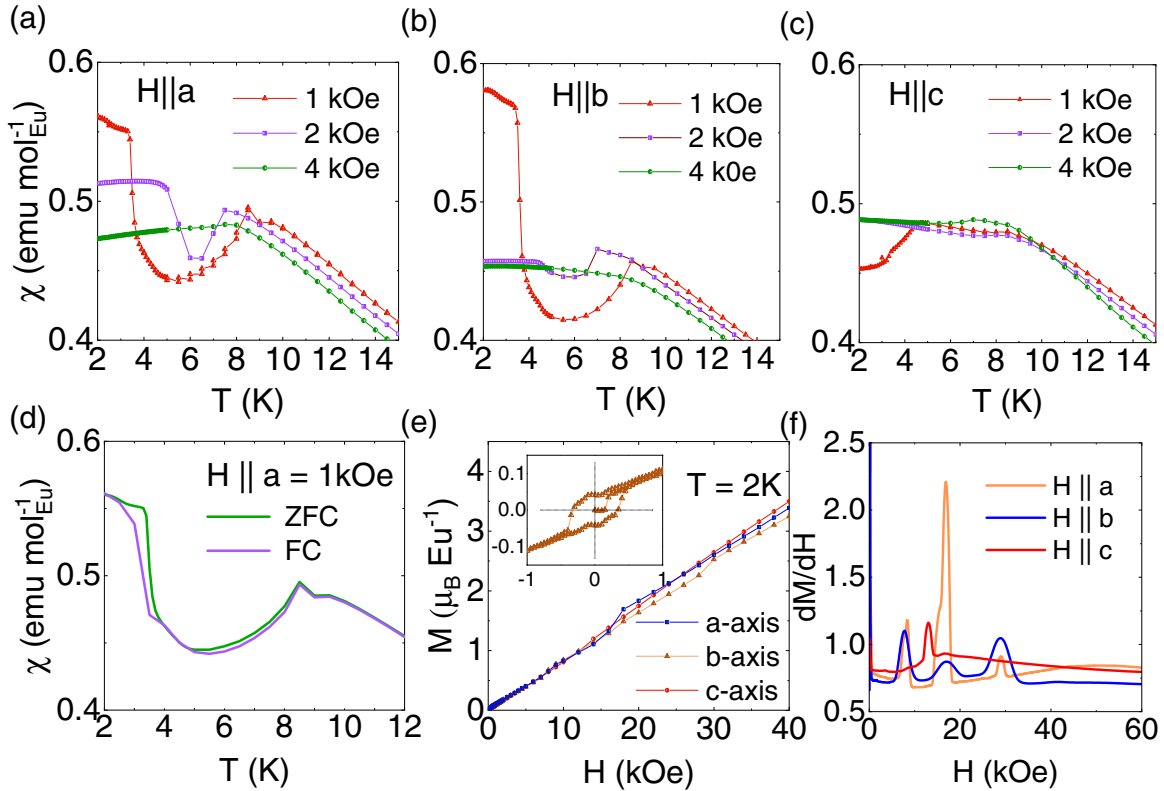


FIG. 2. (a) Low temperature susceptibility in the a axis. (b) Low temperature susceptibility in the b axis. (c) Low temperature susceptibility in the c axis. (d) Zero-field and field-cooled magnetization curves. (e) Low temperature anisotropic magnetization, zero-field cooled, with the inset showing the low-temperature region with hysteresis for $H \parallel b$ around $H = 0$. (f) Derivative with respect to field taken from (e) shows field induced transitions in the a, b , and c axis.

interactions. Further evidence for the onset of short-range interactions is given by the sharp decrease in χT below $T^* = 30$ K [inset of Fig. 1(c)].

Magnetic susceptibility and magnetization (M) measurements provide further insight into the magnetic state of $\text{Eu}_{11}\text{InSb}_9$. The magnetic transitions found in Figs. 2(a)–2(c) are suppressed with increasing field applied along each of the three axes, once again indicative of antiferromagnetic character. Magnetic hysteresis is not evident between zero-field and field-cooled measurements at T_{N1} and T_{N2} for field applied along the a axis, but weak hysteresis is present at T_{N3} [see Fig. 2(d)]. Consequently, a small hysteresis is also observed in a magnetization loop at 2 K, shown in the inset of Fig. 2(e). At a minimum, these results indicate the absence of spin-glass or hard ferromagnetic order. More generally, the temperature dependence of the magnetic susceptibility for $H \parallel a, b$ upon approaching T_{N3} from above and its saturation below T_{N3} reflect a clear change in the nature of magnetic order. Ferrimagnetic or spin-canted order are possible candidates. Additionally, the flattening of low-temperature susceptibility data below T_{N1} and T_{N2} initially suggests that the c axis is the hard magnetization axis, but field-induced transitions along all three axes are observed in dM/dH plots shown Fig. 2(f). Given the presence of six inequivalent Eu sites, it is not surprising to find such complex magnetic order, which hinders magnetic structure determination from magnetization data alone. Magnetic x-ray diffraction measurements would

be valuable to determine the complex magnetic structure of $\text{Eu}_{11}\text{InSb}_9$.

Turning to the electrical properties, Fig. 3(a) shows the temperature dependent electrical resistivity, $\rho(T)$, of $\text{Eu}_{11}\text{InSb}_9$ as measured with current applied in the ab plane. The marked increase in resistivity on cooling is in agreement with the expected semiconducting behavior. The inset of Fig. 3(a) shows $\rho(T)$ in a logarithmic scale to better highlight the presence of distinct resistivity regions, which points to multiple conduction mechanisms. In fact, narrow-gap semiconductors are typically susceptible to defects and impurities, and we find that the electrical resistivity in Fig. 3(a) is in stark contrast to the low-temperature resistivity data for a second sample (s2) shown in Fig. 3(b). This sample is remarkably less insulating than sample s1 and indicates the presence of disorder, defects, or residual flux within the crystals. This result also provides a sensible explanation for the weakly metallic behavior in the electrical resistivity observed previously in $\text{Eu}_{11}\text{InSb}_9$ as measured through a pressed pellet sample that may have contained residual flux [9]. In addition, we cannot rule out the presence of small amounts of hydrogen in these samples, which would be invisible to x rays. The effects of hydrogen in the chemistry of A_5Pn_3 ($A = \text{Alkaline-earth}$ and divalent rare-earth elements, $Pn = \text{As, Sb, Bi}$) has been evaluated in Ref. [17]. Notably, the small change in resistivity on cooling through the magnetic transitions suggests a rather reduced coupling between local moments and

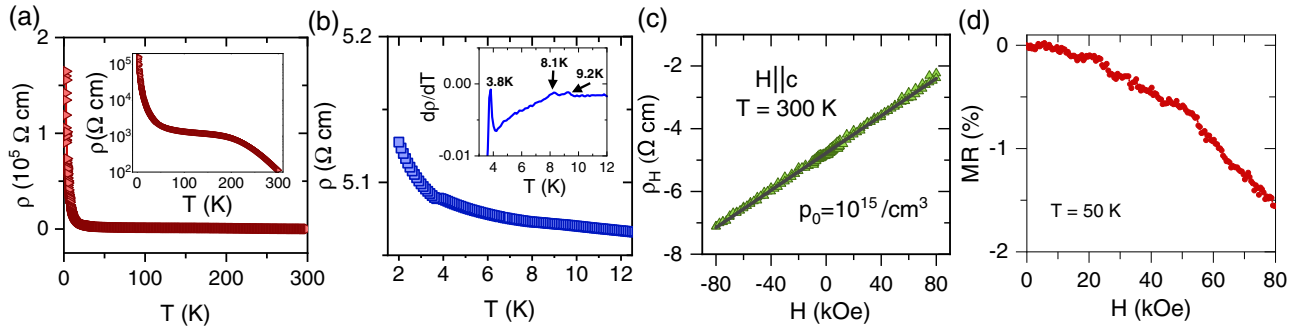


FIG. 3. (a) Electrical resistivity, ρ , versus temperature of $\text{Eu}_{11}\text{InSb}_9$ (sample 1). Inset shows $\log(\rho)$ vs T . (b) Low-temperature electrical resistivity measurements for sample 2. Inset maps transitions identified in both magnetic and specific heat measurements. (c) Hall resistivity ρ_H vs magnetic field of sample 1 measured with field along the c axis. The black line is a linear fit to the data, which agrees with antisymmetrized data and suggests no measurable contribution from longitudinal resistance. (d) Normalized magnetoresistance ($\text{MR} = (\rho(T) - \rho_0)/\rho_0$) as percent for sample 1.

conduction electrons. Small anomalies taken from $d\rho/dT$, shown in the inset of Fig. 3(b), align with those identified from low-temperature magnetic susceptibility and specific heat data.

Field-dependent Hall resistivity data at 300 K, shown in Fig. 3(c), provide valuable information about carrier type and scattering mechanisms in $\text{Eu}_{11}\text{InSb}_9$. The positive Hall coefficient value, $\rho_H/H = R_H = 3 \times 10^3 \text{ cm}^3/\text{C}$, indicates electronic transport dominated by holes. The carrier density is only 10^{15} cm^{-3} , as determined by the single-band expression $1/R_H e$, and is consistent with most narrow-gap semiconductors [24]. Notably, $\text{Eu}_{11}\text{InSb}_9$ has a carrier density two orders of magnitude lower than that of $\text{Eu}_5\text{In}_2\text{Sb}_6$, which was determined to be 10^{17} cm^{-3} at room temperature [8]. The magnetoresistance of $\text{Eu}_{11}\text{InSb}_9$, shown in Fig. 3(d), is also six orders of magnitude smaller than that observed in $\text{Eu}_5\text{In}_2\text{Sb}_6$.

Figure 4 displays an Arrhenius plot, $\ln \rho$ vs $1/T$, wherein a linear fit of the high-temperature linear region ($> 240 \text{ K}$) yields an activation energy of 160 meV, indicative of a relatively narrow gap of 320 meV. In agreement with the inset of Fig. 3(a), distinct regions can be identified, and a simple activation fit alone is inadequate for the characterization of the

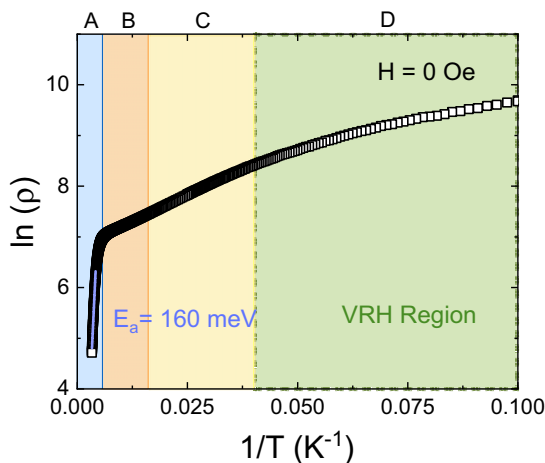


FIG. 4. Arrhenius plot ($\ln(\rho)$ vs. $1/T$) for $\text{Eu}_{11}\text{InSb}_9$. Resistivity data are from Fig. 3(a).

electrical transport at lower temperatures. Narrow-gap semiconductors are typically susceptible to defects and impurities, and the temperature dependence shown in Fig. 4 is consistent with that of a lightly doped semiconductor, i.e., region A exhibits an intrinsic conduction range, whereas regions B, C, and D are consistent with a saturation range of impurity conduction, a freeze-out range, and a hopping conduction regime, respectively [25].

IV. DISCUSSION

The discrepancy between the physical properties of $\text{Eu}_{11}\text{InSb}_9$ and its counterpart $\text{Eu}_5\text{In}_2\text{Sb}_6$ invites a more in-depth comparison between them. Both compounds are Zintl, nonsymmorphic, antiferromagnetic, narrow-gap semiconductors that share the same constituent elements. Thus, one might expect that they share other notable phenomena as well. In particular, colossal magnetoresistance appears to be ubiquitous in low-carrier density Eu^{2+} compounds, such as EuB_6 , EuTe_2 , EuO , and EuIn_2As_2 , to name a few [18–21]. This feature, however, is virtually absent in the work presented here for $\text{Eu}_{11}\text{InSb}_9$. One sensible scenario to explain CMR in this class of materials is the presence of magnetic polarons. For instance, evidence for magnetic polarons in $\text{Eu}_5\text{In}_2\text{Sb}_6$ comes from a collection of experimental results. First, a deviation from the Curie-Weiss law at temperatures much higher than T_N resembles the formation of magnetic polarons in the manganites and is accompanied by the onset of colossal magnetoresistance. Magnetic susceptibility measurements also reveal a ferromagnetic Weiss temperature at high temperatures, which is consistent with the formation of ferromagnetic clusters. Second, at low temperatures a Schottky anomaly in heat capacity measurements combined with a marked decrease in χT above T_N indicate the presence of short-range inter-polaron antiferromagnetic interactions. Finally, microscopic electron spin resonance measurements reveal a linewidth narrowing at high fields, which is consistent with the polaron picture [8].

Though $\text{Eu}_{11}\text{InSb}_9$ also displays complex exchange interactions that lead to a ferromagnetic Weiss temperature at high temperatures and multiple antiferromagnetic transitions at low temperatures, no evidence for magnetic polarons is

observed. The formation of magnetic polarons is largely contingent on two properties: low carrier densities and relatively strong exchange coupling between europium and conduction electron spins [26]. We argue that there must be a lower limit for the carrier density below which magnetic polaron formation is impaired. In fact, the carrier density of $\text{Eu}_{11}\text{InSb}_9$ is significantly lower than that in $\text{Eu}_5\text{In}_2\text{Sb}_6$ and other europium-based CMR materials, which suggests that the formation of ferromagnetic clusters in $\text{Eu}_{11}\text{InSb}_9$ may be hindered by the lack of conduction electrons to self-trap around Eu sites. In addition, a comparison between the crystal structures of $\text{Eu}_{11}\text{InSb}_9$ and $\text{Eu}_5\text{In}_2\text{Sb}_6$ reveals structural elements that provide further explanation for smaller exchange interactions in $\text{Eu}_{11}\text{InSb}_9$. Measuring bond distances between Eu atomic centers and the In-Sb polygons reveals that Eu and In-Sb polygons in $\text{Eu}_{11}\text{InSb}_9$ are, on average, 0.2 Å farther apart than those in $\text{Eu}_5\text{In}_2\text{Sb}_6$. Decreased overlap between f electrons of Eu^{2+} and conduction electrons of the In-Sb polygons could lead to smaller exchange coupling and therefore smaller magnetoresistance.

V. CONCLUSIONS

Here we report the synthesis of $\text{Eu}_{11}\text{InSb}_9$ single crystals and their characterization through thermodynamic and

electrical transport measurements. Our results reveal that $\text{Eu}_{11}\text{InSb}_9$ exhibits a semiconducting ground state with a relatively narrow gap of 320 meV. Magnetic data show that ferromagnetic interactions dominate at high temperature whereas antiferromagnetic correlations set in at low temperatures (<30 K). Unexpectedly, $\text{Eu}_{11}\text{InSb}_9$ showed significantly lower magnetoresistance compared to other related europium-containing compounds, and we attribute this difference to the smaller carrier densities and exchange couplings in $\text{Eu}_{11}\text{InSb}_9$. Our results indicate that $\text{Eu}_{11}\text{InSb}_9$ has potential applications as a thermoelectric material through doping or as a long-wavelength detector due to its narrow gap.

ACKNOWLEDGMENTS

Work at Los Alamos National Laboratory (LANL) was performed under the auspices of the U.S. Department of Energy, Office of Basic Energy Sciences, Division of Materials Science and Engineering. Scanning electron microscope and energy dispersive x-ray measurements were performed at the Center for Integrated Nanotechnologies, an Office of Science User Facility operated for the U.S. Department of Energy Office of Science.

-
- [1] J. M. Tomczak, *J. Phys.: Condens. Matter* **30**, 183001 (2018).
- [2] J. Zheng, H. Zhou, Y. Zou, R. Wang, Y. Lyu, S. P. Jiang, and S. Wang, *Energy Environ. Sci.* **12**, 2345 (2019).
- [3] Y. Hochberg, Y. Kahn, M. Lisanti, K. M. Zurek, A. G. Grushin, R. Ilan, S. M. Griffin, Z. F. Liu, S. F. Weber, and J. B. Neaton, *Phys. Rev. D* **97**, 015004 (2018).
- [4] R. M. Geilhufe, B. Olsthoorn, A. D. Ferella, T. Koski, F. Kahlhoefer, J. Conrad, and A. V. Balatsky, *Phys. Status Solidi (RRL)* **12**, 1800293 (2018).
- [5] M. Z. Hasan and J. E. Moore, *Annu. Rev. Condens. Matter Phys.* **2**, 55 (2011).
- [6] P. Gille and Y. Grin, *Crystal Growth of Intermetallics* (De Gruyter, Berlin, 2018).
- [7] S. M. Kauzlarich, A. Zevalkink, E. Toberer, and G. J. Snyder, *Zintl Phases: Recent Developments in Thermoelectrics and Future Outlook, Thermoelectric Materials and Devices* (RSC Energy and Environment Series, RSC, London, 2017).
- [8] P. Rosa, Yuanfeng Xu, M. Rahn, J. Souza, S. Kushwaha, L. Veiga, A. Bombardi, S. Thomas, M. Janoschek, E. Bauer, M. Chan, Zhijun Wang, J. Thompson, N. Harrison, P. Pagliuso, A. Bernevig, and F. Ronning, *npj Quantum Mater.* **5**, 52 (2020).
- [9] S. Xia, J. Hullmann, S. Bobev, A. Ozbay, E. R. Nowak, and V. Fritsch, *J. Solid State Chem.* **180**, 2088 (2007).
- [10] S. M. Park, S. C. Eun, W. Kang, and S. J. Kim, *J. Mater. Chem.* **12**, 1839 (2002).
- [11] T. Yi, C. A. Cox, E. S. Toberer, G. J. Snyder, and S. M. Kauzlarich, *Chem. Mater.* **22**, 935 (2010).
- [12] S. Kastbjerg, C. A. Uvarov, S. M. Kauzlarich, Y. S. Chen, E. Nishibori, M. A. Spackman, and B. B. Iversen, *Dalt. Trans.* **41**, 10347 (2012).
- [13] S. L. Brock, L. J. Weston, M. M. Olmstead, and S. M. Kauzlarich, *J. Solid State Chem.* **107**, 513 (1993).
- [14] S. Bobev, V. Fritsch, J. D. Thompson, J. L. Sarrao, B. Eck, R. Dronskowski, and S. M. Kauzlarich, *J. Solid State Chem.* **178**, 1071 (2005).
- [15] S. J. Kim, J. R. Ireland, C. R. Kannewurf, and M. G. Kanatzidis, *J. Solid State Chem.* **155**, 55 (2000).
- [16] J. M. De Teresa, M. R. Ibarra, P. A. Algarabel, C. Ritter, C. Marquina, J. Blasco, J. García, A. Del Moral, and Z. Arnold, *Nature (London)* **386**, 256 (1997).
- [17] E. Alejandro Leon-Escamilla and J. D. Corbett, *Chem. Mat.* **18**, 4782 (2006).
- [18] S. Süllow, I. Prasad, M. C. Aronson, S. Bogdanovich, J. L. Sarrao, and Z. Fisk, *Phys. Rev. B* **62**, 11626 (2000).
- [19] H. Yang, Q. Liu, Z. Liao, L. Si, P. Jiang, Z. Liu, Y. Guo, J. Yin, M. Wang, Z. Sheng, Y. Zhao, Z. Wang, Z. Zhong, and Run-Wei Li, *arXiv:2103.02818* (2021).
- [20] M. R. Oliver, J. O. Dimmock, A. L. McWhorter, and T. B. Reed, *Phys. Rev. B* **5**, 1078 (1972).
- [21] A. M. Goforth, P. Klavins, J. C. Fettinger, and S. M. Kauzlarich, *Inorg. Chem.* **47**, 11048 (2008).
- [22] G. Wang, G. Chang, H. Zhou, W. Ma, H. Lin, M. Z. Hasan, S.-Y. Xu, and S. Jia, *Chin. Phys. Lett.* **37**, 107501 (2020).
- [23] J. Blawat, P. Swatek, X. Gui, R. Jin, and W. Xie, *J. Mater. Chem. C* **7**, 12650 (2019).
- [24] J. Chu and A. Sher, *Physics and Properties of Narrow Gap Semiconductors* (Springer, Boston, 2008).
- [25] Boris I. Shklovskii and Alex L. Efros, *Electronic Properties of Doped Semiconductors* (Springer-Verlag, Berlin, 1984).
- [26] A. Kaminski and S. Das Sarma, *Phys. Rev. Lett.* **88**, 247202 (2002).